Fluorescence Lifetime Imaging and Intravascular Ultrasound: Co-Registration Study Using *Ex Vivo* Human Coronaries

Dimitris Gorpas [Member, IEEE],
Department of Biomedical Engineering, University of California, Davis, CA 95616 USA

Hussain Fatakdawala,
Department of Biomedical Engineering, University of California, Davis, CA 95616 USA

Julien Bec,
Department of Biomedical Engineering, University of California, Davis, CA 95616 USA

Dinglong Ma,
Department of Biomedical Engineering, University of California, Davis, CA 95616 USA

Diego R. Yankelevich,
Department of Biomedical Engineering and the Department of Electrical and Computer Engineering, University of California, Davis, CA 95616 USA

Jinyi Qi [Fellow, IEEE], and
Department of Biomedical Engineering, University of California, Davis, CA 95616 USA

Laura Marcu
Department of Biomedical Engineering, University of California, Davis, CA 95616 USA

Dimitris Gorpas: dgorpas@ucdavis.edu; Hussain Fatakdawala: hfatakdawala@ucdavis.edu; Julien Bec: jbec@ucdavis.edu; Dinglong Ma: ucdma@ucdavis.edu; Diego R. Yankelevich: yankelev@ece.ucdavis.edu; Jinyi Qi: qi@ucdavis.edu; Laura Marcu: lmarcu@ucdavis.edu

Abstract

Fluorescence lifetime imaging (FLIM) has demonstrated potential for robust assessment of atherosclerotic plaques biochemical composition and for complementing conventional intravascular ultrasound (IVUS), which provides information on plaque morphology. The success of such a bi-modal imaging modality depends on accurate segmentation of the IVUS images and proper angular registration between these two modalities. This paper reports a novel IVUS segmentation methodology addressing this issue. The image preprocessing consisted of denoising, using the Wiener filter, followed by image smoothing, implemented through the application of the alternating sequential filter on the edge separability metric images. Extraction of the lumen/intima and media/adventitia boundaries was achieved by tracing the gray-scale peaks over the A-lines of the IVUS preprocessed images. Cubic spline interpolation, in both cross-sectional and longitudinal

directions, ensured boundary smoothness and continuity. The detection of the guide-wire artifact in both modalities is used for angular registration. Intraluminal studies were conducted in 13 *ex vivo* segments of human coronaries. The IVUS segmentation accuracy was assessed against independent manual tracings, providing 91.82% sensitivity and 97.55% specificity. The proposed methodology makes the bi-modal FLIM and IVUS approach feasible for comprehensive intravascular diagnosis by providing co-registered biochemical and morphological information of atherosclerotic plaques.

Index Terms

Fluorescence lifetime imaging (FLIM) image denoising; intravascular ultrasound (IVUS); multimodal intravascular imaging; segmentation

I. Introduction

CARDIOVASCULAR disease is the leading cause of death in every industrialized nation and developing country [1]. The past decade has witnessed enormous progress in the understanding of the pathophysiological nature of atherosclerosis, which begins with endothelial dysfunction and ends with the impact of inflammation as major factors of the disease pathogenesis [2]–[4]. However, this knowledge cannot be translated into clinical practice, since the current diagnostic tools rely primarily on anatomical information and are focused mostly on stenosis, the cause of stable angina. Sudden acute cardiac events however, are caused by the rupture of unstable atherosclerotic plaques, which cannot be assessed by the current clinical systems as they do not provide comprehensive information about plaque composition. Despite the advances in high-end imaging systems that are available nowadays to interventional cardiologists, there still exists a need for an effective multimodal technique able to provide registered structural and biochemical information of atherosclerotic plaques [5]. Such a technique has the potential to assist cardiologists to interpret more efficiently the complex features of atherosclerotic plaques and thus to better assess the plaque susceptibility to rupture.

Time-resolved fluorescence spectroscopy (TRFS) and fluorescence lifetime imaging (FLIM) have demonstrated potential for providing information on plaque biochemical composition, associated with plaque vulnerability. Recent studies have shown the application of these fluorescence techniques for detection of plaques with thin fibrous cap and discrimination of lipid-rich and inflamed lesions [6], [7]. Moreover, lifetime measurements do not rely on absolute intensity values and are independent of many factors that affect intensity based measurements, such as the concentration of the fluorophores or the distance between the lumen surface and the collection fiber. This makes TRFS and FLIM very robust in describing the biochemical composition of tissue [8].

Intravascular ultrasound (IVUS) is a well established imaging modality for *in vivo* structural assessment of coronary plaques. It is capable of imaging and quantification of morphological features, such as the cross-section lumen area, the thickness of the intimal layer, the spatial distribution of the plaque, and outward remodeling of the vessel [9]. Efforts to extract plaque composition information from IVUS data have also been reported using

radiofrequency analysis to generate virtual histology IVUS (VH-IVUS) images. [9], [10]. However, IVUS is a technique targeting the structural properties of plaques and cannot provide reliable biochemical information. As a result, recent research efforts have focused on investigating the possibility of combining IVUS data with modalities that are capable of providing such information, such as near-infrared spectroscopy (NIRS) or intravascular near-infrared fluorescence molecular imaging (NIRF) [5], [11]–[13]. Towards this direction, our group has also reported on the prospects of using FLIM to complement IVUS measurements [14] and has developed a bi-modal catheter, integrating an intravascular ultrasound (IVUS) and a fiber-based fluorescence lifetime imaging (FLIM) system [15], [16].

The greatest challenge in mapping FLIM derived biochemical or spectroscopic features on IVUS images is the delineation of the lumen/intima interface from IVUS data. This process is known as IVUS segmentation and can be extended to the extraction of the media/adventitia boundaries [17] as well, allowing the delineation of all three anatomic layers of the artery. A large number of approaches, automated or semiautomated, which attempt to address this problem are reported in the literature. In general, the proposed IVUS segmentation approaches can be categorized in three types, according to a review paper of this field [17], i.e., the direct detection of borders [18], the boundary extraction after a preprocessing step for blood speckle noise removal [19] and the segmentation methods based on supervised classification of lumen area versus the blood-free regions of the IVUS images [20]. Similar categorization of IVUS segmentation approaches is also provided in [21], where the methods and outcomes of the MICCAI 2011 Computing and Visualization for (Intra) Vascular Imaging (CVII) workshop are summarized.

Although this problem has been extensively investigated, and several fully automated approaches have been described [17], [18], [21], many applications are still based on manual or semiautomated IVUS segmentation [22], [23]. The IVUS segmentation challenge has also been encountered in multimodal NIRS and IVUS imaging, where the most common representation is by wrapping the 2-D NIRS data on the perimeter of the IVUS frames, expressed in Cartesian coordinates [13], [24].

The goal of this study is to demonstrate the feasibility of co-registering FLIM data, which provide information on plaque biochemical composition, with the structural information derived from IVUS pull-backs. The current study extends on the preliminary results [25] showing the ability of segmenting the lumen/intima and media/adventitia boundaries using a combined cross-sectional and longitudinal A-line peak detection and addressing four critical aspects required for accurate plaque quantification and co-registration of bi-modal FLIM-IVUS data. These are: 1) extraction of the IVUS lumen/intima boundary; 2) extraction of the IVUS media/adventitia boundary; 3) angular registration between FLIM and IVUS; and 4) mapping of FLIM data onto the luminal surface.

Through the first two steps the entire plaque area is delineated, providing the luminal surface, which is useful for geometrical assessment of the lumen, and the outer vessel surface, which is valuable for quantifying the plaque burden. Moreover, the latter two aspects of the methodology described here are essential for the solution of the FLIM/IVUS

co-registration problem. Once the relative angular position of FLIM fiber and IVUS transducer is identified, the 2-D FLIM data can be mapped onto the luminal surface. This surface becomes available after the lumen/intima segmentation. Combining all the information that is derived from these four aspects, it becomes possible the future development of plaque assessment methodologies, based on combined biochemical and structural data.

II. Materials and Methods

Fig. 1 presents the block diagram of the proposed methodology for the co-registration of FLIM and IVUS data and consists of five steps: multimodal data acquisition, image formation, IVUS segmentation, guide-wire detection and mapping of the FLIM data onto the lumen/intima interface. Each step is highlighted with a different color in Fig. 1 and will be described in the following paragraphs. All algorithms were implemented using Matlab 2013a (MathWorks Inc.).

A. Multimodal Data Acquisition

1) Bimodal Flim-IVUS System—The operational principle of the FLIM system has been previously described in detail elsewhere [15], [16]. Briefly, the intravascular FLIM was enabled by a custom 0.22 NA 300 μm core silica side-viewing optical fiber. The proximal end of the fiber was connected to a wavelength selection chamber, equipped with four bandpass filters to split the collected signal into four different spectral bands for faster acquisition. The respective central wavelength/bandwidth of each channel was 390/40 nm (channel 1), 452/45 nm (channel 2), 542/50 nm (channel 3), and 629/53 nm (channel 4) and their selection was based on the fluorescence emission from collagen, elastin, lipoproteins, and porphyrin correspondingly. Each band was coupled into dedicated delay fibers of different lengths and finally into a single microchannel plate photomultiplier. The excitation source was a fiber laser emitting 20 ps pulses at 355 nm with a variable repetition rate up to 1 MHz. The FLIM fiber was integrated into a custom made bimodal catheter along with a commercial 40 MHz IVUS 3 Fr catheter (Atlantis SR Pro, Boston Scientific, Marlborough, MA, USA) coupled to an acquisition system (iLab, Boston Scientific, Marlborough, MA, USA) [15], [16].

2) Data Acquisition—The data acquisition from these two systems was based on sequential pull-back measurements, initially from FLIM and then from IVUS, over the same imaging section (22 mm maximum distance). The FLIM fiber was rotated at 1200 rpm and 2mm/s pull-back speed, with four consecutive measurements being averaged. With 2.8° angular sampling interval, a full rotation of the fiber consisted of 125 angular steps. This combination of pull-back and rotational motion resulted into a helical scan with 0.1 mm longitudinal travel per fiber revolution. The laser excitation source was set to 10 kHz repetition rate. IVUS had a rotation speed of 1800 rpm and imaging was performed using the same pull back speed as FLIM. With 1.4° angular sampling interval, a full rotation of the transducer consisted of 256 angular steps and 0.07 mm longitudinal travel per transducer rotation. The pull-back scanning principle is depicted in Fig. 2(a) for FLIM and in Fig. 2(c) for IVUS.

The bi-modal data used in this study were obtained from FLIM and IVUS measurements on 13 anterior descending human coronary artery specimens. For data acquisition, the artery specimens were fastened over two luers, using surgical suture with a 0.014 in guide-wire inserted into the arteries. The samples were mounted into a custom built holder on sliders to adjust for varying artery lengths. The two luers also served as markers in the acquired data, ensuring that both modalities were imaging the same distance. The specimens were immersed in phosphate buffered saline bath, maintained at 37 °C, during measurements.

B. Image Formation

1) Flim 2-D Maps—Four fluorescence transient pulses, one for each channel of the FLIM system were acquired at each position of the side-viewing fiber. These pulses were analyzed to obtain fluorescence intensity and lifetime values [26]. Briefly, the fluorescence intensity was obtained by integrating the fluorescence transient pulse over time. Moreover, each transient pulse was a convolution of the fluorescence impulse response function (fIRF) and the instrument response function (iIRF) [8]. The latter was experimentally measured and through a constrained least-square deconvolution process, the fIRF, $\hat{h}(k)$, was approximated [26]. The average lifetime values, $\hat{\tau}_{avg}$, were then estimated by

$$\hat{\tau}_{avg} = \frac{\delta t \cdot \sum_{k=0}^{N-1} k \cdot \hat{h}(k)}{\sum_{k=0}^{N-1} \hat{h}(k)} \quad (1)$$

where δt is the sampling interval and k the sampling point.

After estimating the integrated intensity and the average lifetime values for every angular position of the fiber and for the entire pull-back sequence, these quantities were mapped into 2-D matrices. Each column of these matrices corresponded to a revolution of the fiber or FLIM frame, while each row corresponded to a single angular position. Based on this approximation it was possible to estimate the position of each frame along the pull-back distance. An example is shown in Fig. 2(b) depicting lifetime values of the first channel of the FLIM system (390/40 nm). Similar maps were formulated for both intensity and lifetime values from all four channels.

2) IVUS Frames—Data acquired with the IVUS system were transformed from A-line scans to images in polar coordinates (B-mode frames), Fig. 2(d), where each row corresponds to a distance from the center of the catheter and each column corresponds to an angular position of the transducer. The 8-bit intensity value of each pixel in Fig. 2(d) corresponds to the positive envelope of the acquired radio-frequency signal, followed by log compression. A stack of IVUS frames was created for the same pull-back distance as that in FLIM.

C. Segmentation of the IVUS Images

The co-registration between FLIM and IVUS data requires the mapping of the fluorescence information onto the lumen/intima interface, which can be extracted from IVUS. Moreover, the optimum geometrical characterization of the plaque requires not only the lumen/intima

interface, but also the media/adventitia layer, also known as external elastic lamina (EEL). Therefore, an accurate segmentation of IVUS images is critical.

The method proposed in this study fells into the first two categories of IVUS segmentation approaches [17]: the direct detection of borders, the boundary extraction after a preprocessing step for blood speckle noise removal. Nevertheless, our method presents some fundamental differences from existing IVUS segmentation methods. First, the preprocessing step described in this paper is based on a combination of Wiener [27] and morphological filtering [27]–[29]. Most existing approaches rely on either the median [30] or the anisotropic diffusion filtering [31]. However, both these filters introduce blurring to the region boundaries, decreasing the accuracy of the final segmentation outcome. The filters applied in this study, however, are very robust in preserving the sharpness of the boundaries.

Second, the proposed IVUS segmentation approach is based on combined cross-sectional and longitudinal A-line constrained peak detection. This way, instead of tracking the boundaries inside each cross-sectional IVUS image [31], we constrain the possible locations of the edges of each A-line in regards to the locations of the previous A-lines and frames, succeeding into minimizing the outliers that affect the final segmentation result. Finally, many of the IVUS segmentation approaches in literature are applied to the compressed gray-scale images, transformed in cartesian coordinates, which are provided from the commercial IVUS systems [18], [31]. The algorithm described in the following sections, depends on the acquisition of the radio-frequency signals and is applied to the polar coordinates of the IVUS data.

1) IVUS Image Preprocessing—The input polar images were dominated by noise, even in the absence of blood, causing false boundary detection from direct segmentation approaches. In order to smooth the images, a preprocessing algorithm was developed based on the combination of a denoising filter, a pixel separability filter and a smoothing filter.

The IVUS image preprocessing algorithm was initiated with the application of the Wiener filter, also known as filter of minimum mean square error (MSE) [27]. This is a linear, spatially invariant, filter that considers both image and noise to be random variables. Under this framework, the Wiener filter minimizes the mean square error between the noise-free image and its approximation. The restored image was approximated in the frequency domain by

$$F(u,\upsilon) = \left[\frac{1}{D(u,\upsilon)} \cdot \frac{|D(u,\upsilon)|^2}{|D(u,\upsilon)|^2 + \frac{S_n(u,\upsilon)}{S_f(u,\upsilon)}} \right] \cdot G(u,\upsilon) \quad (2)$$

where $D(u,\upsilon)$ is the degradation function, $|D(u,\upsilon)|^2 = D^*(u,\upsilon) \cdot D(u,\upsilon)$, with $D^*(u,\upsilon)$ being the complex conjugate of $D(u,\upsilon)$, $S_n(u,\upsilon)$, and $S_f(u,\upsilon)$ are the power spectra of the noise and the noise-free image, respectively, [27], [28]. The image in frequency domain is denoted by $G(u,\upsilon)$, and (u,υ) are the frequency coordinates.

From (2) it is apparent that the application of this filter requires some knowledge about the noise type and the noise-free image. In this study, the inherited noise was considered to

follow a Gaussian distribution, with its mean and variance being estimated from the acquired image. Moreover, due to the absence of the noise-free image, its power spectrum was approximated by the power spectrum of the input gray-scale image [28]. Finally, the degradation function was approximated with the spatial filter "unsharp," which, despite its name, is usually applied in cases where edge sharpening is required [27]. The outcome of the Wiener filter application to the IVUS B-mode frame in Fig. 3(a) is shown in Fig. 3(b).

Following the image denoising, an edge enhancement filter was applied to strengthen all the pixels with a high possibility of being boundaries. This algorithm was based on the pixel separability metric [19], [32], [33]

$$\eta = \frac{s_b^2}{s_T^2} \quad (3)$$

$$s_b^2 = n_1 \cdot \left(\overline{P}_1 - \overline{P}\right)^2 + n_2 \left(\overline{P}_2 - \overline{P}\right)^2 \quad (4)$$

$$s_T^2 = \sum_{i=1}^{N} \left(P_i - \overline{P}\right)^2 \quad (5)$$

where $\overline{P}_1$ and $\overline{P}_2$ were the mean values of the intensities within two neighboring regions and n_1 and n_2 were the corresponding number of pixels. $\overline{P}$ was the mean intensity value of the two regions, with a total number of $N = (n_1 + n_2)$ pixels. In this paper, the two neighboring regions corresponded to two vertically aligned tangent windows in the IVUS image.

More specifically, for the case of the lumen/intima segmentation the window sizes were 10 × 3 pixels, or 0.04 mm × 4.2°, as assigned in the algorithm. Larger windows would result into false boundary detection, as low intensity features from the intima would be removed. Also, adventitia usually presents high intensity levels, and to ensure that only these edges were enhanced, the applied pixel separability windows were equal to 30 × 5 pixels or 0.1 mm × 7°. Although the size of these windows was hard-coded in the algorithm, the expression in polar coordinates (instead of pixels), can make their size applicable to different IVUS acquisition protocols.

For each case, the two windows scanned the image and assigned a separability value to the central pixel of their common edge, which was relatively large close to the edges and small in uniform gray-scale areas. Additionally, this metric was weighted with consideration of the structure present in the IVUS image [19], [34]. Fig. 3(c) shows an example of this metric for all the pixels of the B-mode polar image in Fig. 3(b). This metric successfully highlighted all the edge candidates, but it also highlighted the edges of some smaller image features, especially within the intima.

The final step of the IVUS image preprocessing was the image smoothing, obtained by applying sequential erosions, followed by image reconstructions. This process is widely known as alternating sequential filtering (ASF) [27]–[29]. The reconstruction scheme used was the morphological reconstruction by dilation of a gray-scale mask image *f* by a gray-

scale marker image g, defined as the geodesic dilation of g with respect to f. In this work $g = f \ominus B$ and for scale 1 it is expressed as $D_f^{(1)}(f \ominus B) = ((f \ominus B) \oplus B) \bigwedge f$, where $\wedge$ denotes the point-wise minimum operation, $\oplus$ denotes the dilation filter and $\ominus$ denotes the erosion filter and B is the filters structured element [27], [28]. This operator was applied sequentially to the gray-scale IVUS separability metric images and to their complement, for each scale, treating symmetrically the image foreground and background and thus accomplishing image simplification and contrast enhancement, without affecting the positions of the boundaries. The sequential application of this operator generated the applied nonlinear smoothing filter

$$\psi_{ASF}(f) = b_r(a_r(\cdots(b_2(a_2(b_1(a_1)))))) \quad (6)$$

with the smoothing progressively increasing from the scale of size 1 up to a maximum scale r. In (6) $a_1(f) = \left[D_f^{(1)}(f \ominus B)\right]^c$ and $b_1(f) = \left[D_f^{(1)}(a_1(f))\right]^c$, where c indicates the complement of the operator outcome.

Fig. 3(d) shows the outcome of the ASF after being applied to Fig. 3(c). The ASF retained most of the edges present in the pixel separability metric image, while removing all relatively small artifacts that the pixel separability metric introduced, especially in the intima region. Moreover, intima and adventitia regions now present uniform pixel intensity values.

The two parameters that affect the application of the ASF filter, as can be seen in (6), are the scale and the structured element. For this study it was found that a scale equal to 2 can efficiently smooth the gray-scale pixel separability metric image, without removing any of the image features, like the high intensity of the adventitia region. Higher scales would flatten the adventitia so that its distinction from intima would become impossible. Furthermore, in such a scale the ASF is independent of the structured element shape. In this paper, we chose the circular shape; nevertheless the outcome of the filter is similar for any 2-D shape. Finally, because the selection of the scale is related to the spatial resolution of the IVUS data, we have linked the scale to this metric. More specifically, the chosen scale corresponds to a circle of diameter equal to five pixels, or for the current IVUS system to 0.02 mm vertical or 7° horizontal.

As aforementioned, the applied filters do not blur and/or shift the true boundaries of the IVUS images. This is demonstrated in Fig. 3, where the true boundaries have been overlaid in the results of all the image preprocessing steps. Comparing Fig. 3(a), which is the original gray-scale image, with Fig. 3(d), which is the outcome of the ASF filtering, one can observe that in the final image the boundaries are in the same exact location as in the original, with significantly less noise in the neighboring regions.

2) IVUS Segmentation—The developed IVUS segmentation approach was based on combined cross-sectional and longitudinal A-line peak detection. From each IVUS A-line, $I(d, p)$, where d is the distance from the transducer and $p = 1, \ldots, 256$ are the angular steps, all the gray-scale intensity peaks were detected as local maximums. Minor peaks were removed by thresholding at the median of all the intensities in each A-line. The K detected peaks were further reduced by extracting only those that follow zero intensity pixels

$$E_k = \begin{cases} d_k, & \text{if } k = \underset{i \subseteq [1,K], d_i \geq z_k}{\arg \min} (d_i - z_k) \\ 0, & \text{otherwise} \end{cases} \quad (7)$$

where $\mathbf{E} = [E_k]$ is a vector of length equal to the number of peaks, K, $k = 1, \ldots, K$ is the peak index, and d_k the distance from the transducer, in pixels, of each detected peak. z_k denotes the distance from the transducer of the last zero intensity pixel before the kth peak and for the pth A-line it is

$$z_k = \max \left\{ \arg \min_{d \in [1, (d_k - 1)]} [I(d, p)] \right\}. \quad (8)$$

The four vessel areas that can be seen in an IVUS image, the lumen, intima, media, and adventitia, can also be distinguished when inspecting a single A-line, Fig. 4(a). Based on this assumption, the lumen/intima edge in the first A-line of the considered frame was the first peak obtained by (7), while from the remaining peaks, the one with the maximum intensity was assigned as the EEL edge, Fig. 4(b). Narrow peaks, where the distance between the last zero intensity pixel before the peak and the first one after the peak was relatively small, were discarded as they corresponded to small artifacts which were not fully compensated for during the image preprocessing. Moreover, if after the assignment of the lumen boundary there was no other peak detected by (7), then the last pixel of intima was assigned as the EEL edge. This often occurs near calcification regions. Finally, when no peak was detected by (7), for example in the case of side branches, then this A-line was skipped and the process repeated for the following A-line.

Once the lumen/intima and EEL edges were identified in one A-line, then the corresponding edges in all the other A-lines of the first frame were defined as

$$\text{Edge}_p = \begin{cases} E_k, & \text{if } d_k \in [(\text{Edge}_{p-1} - w), (\text{Edge}_{p-1} + w)] \\ \text{Edge}_{p-1}, & \text{otherwise} \end{cases} \quad (9)$$

where Edge_p is the edge of the pth A-line, Edge_{p-1} is the edge from previous A-line, E_k are the peaks evaluated by (7) and d_k their locations in pixels. In other words, through (9) is identified the A-line peak, which is located within $\pm w$ distances from the detected edge of the previous A-line, Fig. 4(b). For the subsequent frames, the edge tracking retained the formalism of (9), with the difference that Edge_p now corresponds to a single A-line of the pth frame, whereas Edge_{p-1} corresponds to the same A-line in the previous frame.

Under this modus the continuity and smoothness of the detected boundaries was preserved in both the cross-sectional and longitudinal directions. Furthermore, the application of (9) ensured that in case of artifacts like the guide-wire or side-branches, the segmentation will retain the curvature of the previous regions.

The selection of the parameter w, which defines the region within which the A-line peaks are searched, was based on the observation that both lumen/intima and EEL boundaries on

each IVUS frame are connected edges. Similarly, subsequent IVUS frames should present continuous and smooth boundaries. Thus, large jumps of the edge locations either correspond to the guide-wire artifact or to side branches. In order to avoid including these artifacts into the segmentation process, this parameter was set equal to 0.2 mm for both lumen/intima and EEL boundaries. Similarly to the structured element and pixel separability windows definition, expressing w in terms of metrical dimensions, rather than pixels, ensure that the algorithm could be applied to different IVUS acquisition protocols.

The final step during the segmentation process was the cubic splines interpolation of the extracted boundaries. This was applied twice, initially for each B-mode polar image, so to ensure smoothness in the segmentation of each frame, and then for a unique A-line across the entire pull-back sequence, ensuring continuity along the pull-back direction.

3) Segmentation Assessment—IVUS segmentation was assessed by comparing results to two independent manual tracings of randomly selected frames. The quantitative error indexes that were calculated included mean signed border positioning error (d_s), mean unsigned border positioning error (d_u) and root mean square (rms) border positioning error. All these indexes are defined in [18]. The positioning error indexes were quantified from the polar coordinates of the segmented boundaries and the distances for each angular position between the boundary pixels derived by subtracting the proposed algorithm outcomes from the manually traced edges. Moreover, the Hausdorff distances were also calculated from the B-mode IVUS images, expressed in cartesian coordinates, while the linear regression between manual and automated tracings was also estimated. Finally, the sensitivity and specificity of the proposed algorithm in detecting the plaque area were evaluated in regards to the reference segmentations.

Additionally, the same figures of merit were used to compare the boundaries extracted from the proposed methodology and the manually assisted segmentation results from commercially available software (iMap, Boston Scientific, Marlborough, MA, USA).

D. Guide-Wire Detection and Data Co-Registration

The current version of the bimodal catheter is based on the sequential pull-back data acquisition from the two modalities, over the same imaging window [15]. Under this modus, the longitudinal distance was the same for both IVUS and FLIM and thus the co-registration along the pull-back direction was straightforward. Also, since each modality was rotating independently from the other, the angular registration was implemented based on a feature that was present in both IVUS and FLIM. This feature was the guide-wire artifact, which can be seen in Fig. 2(d) as the bright artifact inside the lumen area of the IVUS frame and in Fig. 2(b) as the low lifetime line for the FLIM data.

The tracking of the guide-wire in FLIM data was based on the fact that guide-wire used in the study does not fluoresce under 355 nm excitation. Thus, tracking the lowest fluorescence intensity values for all FLIM frames provided the angular position of the guide-wire. The channel presenting the highest fluorescence intensity among the four channels of the FLIM system was selected to ensure better accuracy for guide-wire extraction.

The guide-wire artifact was identified as the area with the highest intensity values inside the lumen. Although this assumption was true for most of the IVUS frames, there were cases where other artifacts inside the lumen, like reflectance artifacts from the catheter sheath, presented higher intensity than the guide-wire. To address this issue, the lumen area from all the IVUS frames for a given pull-back sequence was averaged and the resulted image was thresholded to the mean value of its nonzero pixels. This binary image was used as a mask for the detection of the guide-wire in all the IVUS frames by tracking the highest intensity pixel inside the mask area. The resulting pixel coordinates were smoothed in radial and longitudinal directions removing all instances that significantly deviate from their neighboring locations and ensuring that the guide-wire preserved a linear shape.

After extracting the guide-wire position in both modalities, their co-registration was implemented by rotating each FLIM frame, so that its guide-wire instance match the position of the guide-wire in the corresponding IVUS frame. With this transformation, each FLIM image pixel corresponded to an IVUS A-line, and, by having segmented lumen/intima boundaries, the distance from the center of the catheter could be assigned to this pixel, providing three-dimensional attribute to the 2-D FLIM data.

The co-registration assessment was addressed through measurements of a phantom consisting of eight capillaries every 45° around the catheter and located in parallel to the pull-back direction. Green and pink fluorescent paint (Scribbles, Fresno, CA, USA) was used to mark the capillaries. Seven capillaries were filled with the pink fluorescent paint, emitting mainly in channel 4 (629/53 nm), while the eighth one was filled with the green fluorescent paint, emitting mainly in channel 3 (542/50 nm) and serving as the reference capillary. A wire close to this capillary was also serving as the reference marker for the IVUS images. The co-registration was then assessed by inspecting the angular position of the emitted fluorescence in relation to the capillaries position as detected by the IVUS system.

III. Results

A. IVUS Segmentation

The automated segmentation algorithm developed here was applied to pull-back sequences from all 13 coronary segments that included a total of 2102 frames. Six representative frames, with the corresponding segmentation results superimposed, are shown in Fig. 5(a)–(c) and in Fig. 5(e)–(g). The corresponding longitudinal views of the two pull-back sequences are shown in Fig. 5(d) and (h).

The segmentation results shown in these figures demonstrate the functionality of the proposed segmentation algorithm. As it can be observed, variations in the echogenicities of different regions in the IVUS images such as shadowing behind calcification areas, hypoechoic lipid pools, side-branches or guide-wire artifacts, do not affect the segmentation process. This is mostly due to the edge tracing window *w* which has been defined in (9) in Section II-C. If no edge candidate can be found within the area delimited by this window in a specific A-line of a certain frame, then this edge location is approximated by using the corresponding locations of the previous A-lines and/or frames.

For example, the lumen/intima boundary of Fig. 5(b) does not follow the boundaries of the side-branch, which are clearly visible in this figure. Similarly, the EEL boundary of Fig. 5(f) does not converge to the calcification outer boundaries. Instead, it retains a curvature that matches the curvature of the noncalcified regions. The latter is more obvious in Fig. 5(d), where it can be observed that once the calcified area starts, the EEL boundary tends to retain the location of the corresponding boundary of the previous frame, while the tracing is re-initiated after the calcification.

The linear regression analysis (Fig. 6) revealed that the results of the proposed segmentation were strongly correlated with the manual segmentation, yielding slopes close to 1 and intercepts close to 0 for both lumen/intima and EEL boundaries ($p \ll 0.01$). For this analysis, the distance, in mm, between the boundaries resulting from each method and the transducer was used. The manual segmentation, used for assessing the proposed algorithm, was estimated as the mean of two independent manual tracings, which corresponds to the best approximation of the boundaries. Table I summarizes all the quantitative error indexes for lumen/intima segmentation results. The corresponding indexes for EEL segmentation are given in Table II.

As it can be seen in Tables I and II, all the indexes estimated for the assessment of the proposed methodology are equivalent to the corresponding interobserver indexes, either in a fully manual segmentation approach or in the manually assisted iMap segmentation. This observation is further validated when the Haussdorff distances are estimated per frame, between the two manual segmentations, the proposed and the manual ones, and the iMap and the manual segmentations. The corresponding mean values of the Haussdorff distances from all the frames are 0.21 ± 0.10 mm, 0.19 ± 0.10 mm and 0.20 ± 0.10 mm for the lumen/intima and 0.25 ± 0.20 mm, 0.33 ± 0.20 mm and 0.24 ± 0.15 mm for the EEL boundaries, respectively. Moreover, the sensitivity of the segmentation approaches, considering the mean of the manually traced boundaries from two users as true, is 93.27% for the first user, 94.27% for the second user, 91.82% for the proposed automated method and 88.38% for the manually assisted iMap segmentation. The corresponding specificity values are 99.30%, 99.21%, 97.55%, and 98.48%.

The assessment of the proposed automatic segmentation method clearly shows potential to replace the golden standard manual segmentation, or any other manually assisted method, without any decrease in the accuracy of plaque delineation. Also, these results are in good agreement with similar applications in [18]. However, direct and quantitative comparisons with current state-of-art segmentation approaches will become feasible once current multimodal FLIM/IVUS catheter is translated to *in vivo* cases and by using the standardized evaluation methodology described in [21].

B. FLIM-IVUS Co-Registration

The co-registration process between FLIM and IVUS data was performed using the lumen/intima boundary from the presented segmentation method. Fig. 7 shows a few representative co-registration results. Fig. 7(a)–(c) depict the mapping of the lifetime values (channel 1 at 390/40 nm) onto the corresponding IVUS frames shown in Fig. 5(e)–(g). Fig. 7(d) and (e) show the intensity and lifetime mapping onto the entire pull-back sequence in a fly-through

mode. The intensity in Fig. 7(d) has been normalized to the maximum intensity value of the entire pull-back sequence. However, the changes of the intensity across the pull-back, or even changes of these values over a single revolution, are not always related to changes in the composition of the plaque. As it is well known, the distance between the fluorophore and the detector, as well as the concentration of the fluorophore, can produce strong variations to the measured intensity. This, of course, does not mean there is a change in the plaque composition.

In comparison, the lifetime values do not depend on the aforementioned distance, and thus can be used to detect changes in the composition of the plaque. This means that the 3-D reconstruction of the luminal surface shown in Fig. 8(a) for the first channel (390/40 nm) and Fig. 8(b) for the second channel (452/45 nm) can become a valuable asset towards the assessment of the composition of the plaque, as has been shown in previous studies of our group [6], [7], that might be difficult to achieve through intensity measurements.

This is, also, the major advantage of FLIM against intensity based measurements, like NIRS. The latter one is strongly depending on the distance between the collection fiber and the luminal surface, as well as on the concentration of the plaque components. For that reason there is a need to correct the acquired NIRS data before any assessment can be made [35]. This issue is also present in the case of the NIRF imaging, where attempts to correct for the distance dependence have been reported by various researchers [22], [36].

The co-registration assessment between the two modalities is shown in Fig. 9. The 2-D maps of fluorescence and IVUS intensities, along the pull-back distance and angular position of the catheter, were used for the display. The angular position of the reference capillary, Fig. 9(b) for FLIM and Fig. 9(e) for IVUS, was used to co-register the two modalities by rotating the FLIM data so that the marker capillary to be on the same angular position for both IVUS and FLIM. In Fig. 9(g) are shown the center lines from both data (dashed lines for FLIM and solid ones for IVUS).

The mean absolute error between the angular positions of the capillaries center lines from both modalities was estimated equal to $2.27° \pm 1.74°$. For the evaluation of Fig. 9 it was ensured that the rotation speed was constant and equal to 1200 rpm for FLIM and 1800 rpm for IVUS. Moreover, it was ensured that both of them were perpendicular to the pull-back path and that they were centered to the catheter. Then this experiment was repeated with both FLIM and IVUS under two stress conditions: catheter bending that caused friction during rotation, and off center acquisition. The resulted mean absolute error in those cases was equal to $17.6° \pm 12.5°$, or $4.9\% \pm 3.5\%$, respectively. This mean absolute error indicates that the co-registration between the two modalities presents high accuracy, despite the nonsimultaneous data acquisition.

IV. Discussion and Conclusion

The bi-modal FLIM and IVUS system can provide the interventional cardiologists combined biochemical and structural information for assessing the atherosclerotic plaque. Accurate segmentation of the IVUS image is essential for proper co-registration of the two data sets.

In this paper we proposed an automated methodology for the segmentation of both lumen/ intima and media/adventitia boundaries. The segmentation was achieved by seeking peaks over every A-line of the B-mode polar images after applying an image preprocessing algorithm to remove noise. The quantitative assessment of the proposed methodology against independent manual boundary tracings indicated high accuracy in the extraction of the desired borders. The proposed algorithm can also be combined with other existing techniques for manual refinement of the extracted boundaries [18]. This is expected to increase the accuracy of the segmentation results and also to address any possible errors due to motion artifacts during *in vivo* IVUS measurements.

For each frame the proposed algorithm requires approximately 9 s for segmenting both boundaries and by considering full resolution of the acquired RF IVUS data. Working towards the adaptation of the algorithm for *in vivo* measurements we will also optimize it to allow quasi-real time segmentation.

Although this segmentation algorithm was developed for *ex vivo* human coronary segments, the same acquisition protocol is expected for the *in vivo* measurements as well. This is due to the fact that the excitation wavelength used for the FLIM data acquisition is strongly absorbed by the blood and thus *in vivo* application of this bi-modal technique requires measurements under blood flushing conditions similar with those used for intravascular OCT [5], [37]. In order to translate the proposed segmentation algorithm to *in vivo* pull-back measurements, parameters optimization will be required due to cardiac and breathing motion, especially in the cases of nongated IVUS measurements.

Moreover, the proposed IVUS segmentation algorithm has been developed for the 40 MHz IVUS 3 Fr Atlantis SR Pro catheter (Boston Scientific, Marlborough, MA, USA) and the required input is the RF-IVUS data, expressed in polar coordinates. This algorithm is based on four parameters: the scale of the ASF filter, the window size of the pixel separability window and the peak location constrain windows per cross-sectional and longitudinal directions. The values of these parameters are currently expressed in metrical dimensions, rather than pixels, thus making them independent of the IVUS acquisition resolution. However, optimization of the four parameters might be required when different IVUS transducers are used.

Finally, during the translation from the *ex vivo* to the *in vivo* measurements, the data acquisition will be optimized through simultaneous FLIM/IVUS scanning, resulting into co-registration at the hardware level. Multimodal intravascular imaging catheters, which perform the co-registration at hardware level, have been developed for other applications, i.e., NIRF/IVUS [36] Such hardware adaptation is essential as the combined cardiac and breathing motion will make the guide-wire based co-registration impractical. This will only require a minor modification to the proposed co-registration methodology: the detection of an image feature will be replaced with a predefined angular delay between the two modalities, and the co-registration process will proceed as described in this paper. Nevertheless, the proposed approach can be accurately applied for the *ex vivo* cases, which is an essential step towards the translation of the bi-modal system into *in vivo* human measurements.

The proposed method makes the bi-modal FLIM and IVUS approach feasible for comprehensive intravascular diagnostic, by providing co-registered biochemical and morphological information about atherosclerotic plaques. However, it can also be extended to other bi-modal imaging systems, like NIRS-IVUS or NIRF-IVUS, and with some modification we expected that it can be applicable to OCT-based imaging data.

Based on the widely accepted claim that the future of intravascular imaging lies within the multimodality [5], the current study is a significant step towards the implementation of such a system. Previous studies of our group have indicated the prospects of FLIM to biochemically assess the atherosclerotic plaques. Through the current study, for the first time in literature, FLIM information is mapped onto the luminal surface as delineated from IVUS pull-back measurements. Providing all this bi-modal information, future works include the development of a classification architecture that would be based on both FLIM and IVUS data to assess the images plaques and the translation of the proposed methodology into *in vivo* human measurements.

Supplementary Material

Refer to Web version on PubMed Central for supplementary material.

Acknowledgment

References

1. Go AS, Mozaffarian D, Roger VL, Benjamin EJ, Berry JD, Borden WB, Bravata DM, Dai SF, F1ord ES, Fox CS, Franco S, Fullerton HJ, Gillespie C, Hailpern SM, Heit JA, Howard VJ, Huffman MD, Kissela BM, Kittner SJ, Lackland DT, Lichtman JH, Lisabeth LD, Magid D, Marcus GM, Marelli A, Matchar DB, McGuire DK, Mohler ER, Moy CS, Mussolino ME, Nichol G, Paynter NP, Schreiner PJ, Sorlie PD, Stein J, Turan TN, Virani SS, Wong ND, Woo D, Turner MB, Assoc AH, Subcomm SS. Heart disease and stroke statistics-2013 update a report from the American heart association. Circulation. 2013; 127:E6–E245. [PubMed: 23239837]

2. Weber C, Noels H. Atherosclerosis: Current pathogenesis and therapeutic options. Nat. Med. 2011; 17:1410–1422. [PubMed: 22064431]

3. Moore KJ, Tabas I. Macrophages in the pathogenesis of atherosclerosis. Cell. 2011; 145:341–355. [PubMed: 21529710]

4. Arbab-Zadeh A, Nakano M, Virmani R, Fuster V. Acute coronary events. Circulation. 2012; 125:1147–1156. [PubMed: 22392862]

5. Suter MJ, Nadkarni SK, Weisz G, Tanaka A, Jaffer FA, Bouma BE, Tearney GJ. Intravascular optical imaging technology for investigating the coronary artery. JACC-Cardiovasc. Imag. 2011; 4:1022–1039.

6. Phipps JE, Sun Y, Fishbein MC, Marcu LA. Fluorescence lifetime imaging classification method to investigate the collagen to lipid ratio in fibrous caps of atherosclerotic plaque. Lasers Surg. Med. 2012; 44:564–571. [PubMed: 22886522]

7. Marcu L. Fluorescence lifetime in cardiovascular diagnostics. J. Biomed. Opt. 2010; 15 011106–011106-10.

8. Lakowicz, JR. Principles of Fluorescence Spectroscopy. 3rd ed.. New York: Springer; 2006.

9. Garcìa-Garcìa HM, Gogas BD, Serruys PW, Bruining N. IVUS-based imaging modalities for tissue characterization: Similarities and differences. Int. J. Cardiovas. Imag. 2011; 27:215–224.

10. Nair A, Kuban BD, Tuzcu EM, Schoenhagen P, Nissen SE, Vince DG. Coronary plaque classification with intravascular ultrasound radiofrequency data analysis. Circulation. 2002; 106:2200–2206. [PubMed: 12390948]

11. Thukkani AK, Jaffer FA. Intravascular near-infrared fluorescence molecular imaging of atherosclerosis. Am. J. Nucl. Med. Mol. Imag. 2013; 3:217–231.

12. Vinegoni C, Botnaru I, Aikawa E, Calfon MA, Iwamoto Y, Folco EJ, Ntziachristos V, Weissleder R, Libby P, Jaffer FA. Indocyanine green enables near-infrared fluorescence imaging of lipid-rich, inflamed atherosclerotic plaques. Sci. Transl. Med. 2011; 3

13. Wentzel JJ, van der Giessen AG, Garg S, Schultz C, Mastik F, Gijsen FJH, Serruys PW, van der Steen AFW, Regar E. In vivo 3D distribution of lipid-core plaque in human coronary artery as assessed by fusion of near infrared spectroscopy-intravascular ultrasound and multislice computed tomography scan. Circ. Cardiovasc. Imag. 2010; 3:E6–E7.

14. Sun Y, Chaudhari AJ, Lam M, Xie HT, Yankelevich DR, Phipps J, Liu J, Fishbein MC, Cannata JM, Shung KK, Marcu L. Multimodal characterization of compositional, structural and functional features of human atherosclerotic plaques. Biomed. Opt. Expr. 2011; 2:2288–2298.

15. Bec J, Xie HT, Yankelevich DR, Zhou FF, Sun Y, Ghata N, Aldredge R, Marcu L. Design, construction, and validation of a rotary multifunctional intravascular diagnostic catheter combining multispectral fluorescence lifetime imaging and intravascular ultrasound. J. Biomed. Opt. 2012; 17:106012. [PubMed: 23224011]

16. Bec J, Ma DM, Yankelevich DR, Liu J, Ferrier WT, Southard J, Marcu L. Multispectral fluorescence lifetime imaging system for intravascular diagnostics with ultrasound guidance: In vivo validation in swine arteries. J. Biophoton. 2013 May.

17. Katouzian A, Angelini ED, Carlier SG, Suri JS, Navab N, Laine AF. A state-of-the-art review on segmentation algorithms in intravascular ultrasound (IVUS) images. IEEE T. Inf. Technol. Biomed. 2012; 16:823–834.

18. Sun S, Sonka M, Beichel RR. Graph-based IVUS segmentation with efficient computer-aided refinement. IEEE Trans. Med. Imag. 2013; 32:1536–1549.

19. Koga, T.; Uchino, E.; Suetake, N. Proc. IEEE Int. Conf. on Fuzzy Syst. (FUZZ-IEEE 2011). Taipei, Taiwan: 2011. Automated boundary extraction and visualization system for coronary plaque in IVUS image by using fuzzy inference-based method; p. 1966-1973.

20. Katouzian A, Baseri B, Konofagou EE, Laine AF. Automatic detection of blood versus non-blood regions on intravascular ultrasound (IVUS) images using wavelet packet signatures. Proc SPIE, Ultrason. Imag. Signal Process. 2008:69200H.

21. Balocco S, Gatta C, Ciompi F, Wahle A, Radeva P, Carlier S, Unal G, Sanidas E, Mauri J, Carillo X, Kovarnik T, Wang CW, Chen HC, Exarchos TP, Fotiadis DI, Destrempes F, Cloutier G, Pujol O, Alberti M, Mendizabal-Ruiz EG, Rivera M, Aksoy T, Downe RW, Kakadiaris IA. Standardized evaluation methodology and reference database for evaluating IVUS image segmentation. Comput. Med. Imag. Graph. 2014; 38:70–90.

22. Mallas G, Brooks DH, Rosenthal A, Nudelman RN, Mauskapf A, Jaffer Fa, Ntziachristos V. Improving quantification of intravascular fluorescence imaging using structural information. Phys. Med. Biol. 2012; 57:6395–6406. [PubMed: 22996051]

23. Jaffer FA, Calfon MA, Rosenthal A, Mallas G, Razansky RN, Mauskapf A, Weissleder R, Libby P, Ntziachristos V. Two-dimensional intravascular near-infrared fluorescence molecular imaging of inflammation in atherosclerosis and stent-induced vascular injury. J. Am. Coll. Cardiol. 2011; 57:2516–2526. [PubMed: 21679853]

24. Madder RD, Steinberg DH, Anderson RD. Multimodality direct coronary imaging with combined near-infrared spectroscopy and intravascular ultrasound: Initial US experience. Catheter. Cardiovasc. Interv. 2013; 81:551–557. [PubMed: 22110009]

25. Gorpas D, Fatakdawala H, Bec J, Ma D, Yankelevich DR, Bishop JW, Qi J, Marcu L. Bi-modal imaging of atherosclerotic plaques: Automated method for co-registration between fluorescence lifetime imaging and intravascular ultrasound data. Proc. SPIE, Photon. Therapeut. Diagnost. X. 2014:892638.

26. Liu J, Sun Y, Qi J, Marcu L. A novel method for fast and robust estimation of fluorescence decay dynamics using constrained least-squares deconvolution with laguerre expansion. Phys. Med. Biol. 2012; 57:843–865. [PubMed: 22290334]

27. Gonzalez, RC.; Woods, RE. Digital Image Processing. 3rd ed.. Upper Saddle River, NJ: Prentice-Hall; 2008.

28. Bovik, AC. Handbook of Image and Video Processing. 2nd ed.. Amsterdam; Boston, MA: Elsevier Academic; 2005.

29. Sofou, A.; Tzafestas, C.; Maragos, P. Proc. IEEE Int. Conf. on Image Process.(ICIP '01). Thessaloniki, Greece: 2001. Segmentation of soilection images using connected operators; p. 1087-1090.

30. Yan J, Liu H, Cui Y. A random walk-based method for segmentation of intravascular ultrasound images. Proc. SPIE, Biomed. Appl. Molec., Structur., and Funct. Imag. 2014:903825–903829.

31. Papadogiorgaki M, Mezaris V, Chatzizisis YS, Giannoglou GD, Kompatsiaris I. Image analysis techniques for automated IVUS contour detection. Ultrasound Med. Biol. 2008; 34:1482–1498. [PubMed: 18439746]

32. Fukui K. Edge extraction method based on separability of image features. IEICE Trans. Inf. Syst. 1995; E78-D:1533–1538.

33. Liu, S.; Wei, J.; Feng, B.; Lu, W.; Denby, B.; Fang, Q.; Dang, J. Proc. IEEE Signal Inform. Process. Assoc. Ann. Summit and Conf. (APSIPA ASC). Hollywood, CA: 2012. An anisotropic diffusion filter for reducing speckle noise of ultrasound images based on separability; p. 1-4.

34. Uchino E, Suetake N, Koga T, Kubota R, Ichiyama S, Hashimoto G, Hiro T, Matsuzaki M. Fuzzy inference-based plaque boundary extraction using image separability for intravascular ultrasound image of coronary artery. Electron. Lett. 2009; 45:451–453.

35. Fard AM, Vacas-Jacques P, Hamidi E, Wang H, Carruth RW, Gardecki JA, Tearney GJ. Optical coherence tomography – near infrared spectroscopy system and catheter for intravascular imaging. Opt. Expr. 2013; 21:30849–30858.

36. Dixon AJ, Hossack JA. Intravascular near-infrared fluorescence catheter with ultrasound guidance and blood attenuation correction. J. Biomed. Opt. 2013; 18:056009–056009.

37. Tearney GJ, Regar E, Akasaka T, Adriaenssens T, Barlis P, Bezerra HG, Bouma B, Bruining N, Cho J-M, Chowdhary S, Costa MA, de Silva R, Dijkstra J, DiMario C, Dudeck D, Falk E, Feldman MD, Fitzgerald P, Garcia H, Gonzalo N, Granada JF, Guagliumi G, Holm NR, Honda Y, Ikeno F, Kawasaki M, Kochman J, Koltowski L, Kubo T, Kume T, Kyono H, Lam CCS, Lamouche G, Lee DP, Leon MB, Maehara A, Manfrini O, Mintz GS, Mizuno K, Morel M-A, Nadkarni S, Okura H, Otake H, Pietrasik A, Prati F, Räber L, Radu MD, Rieber J, Riga M, Rollins A, Rosenberg M, Sirbu V, Serruys PWJC, Shimada K, Shinke T, Shite J, Siegel E, Sonada S, Suter M, Takarada S, Tanaka A, Terashima M, Troels T, Uemura S, Ughi GJ, van Beusekom HMM, van der Steen AFW, van Es G-A, van Soest G, Virmani R, Waxman S, Weissman NJ, Weisz G. Consensus standards for acquisition, measurement, and reporting of intravascular optical coherence tomography studies: A report from the international working group for intravascular optical coherence tomography standardization and validation. J. Amer. Coll. Cardiol. 2012; 59:1058–1072. [PubMed: 22421299]
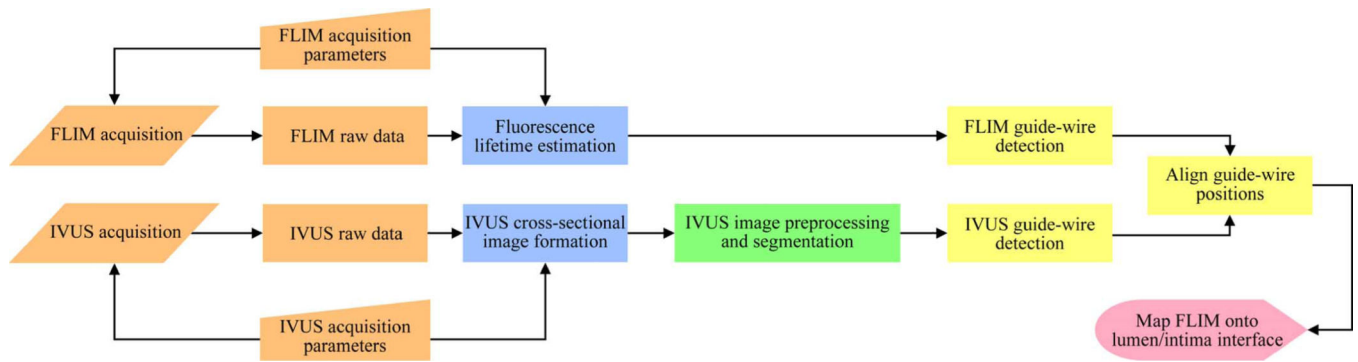
Fig. 1.
Proposed methodology initiates after the acquisition of the multimodal data (orange group) and the formation of the corresponding images (blue group). Algorithmic core of this method is the IVUS segmentation (green block) and the guide-wire detection in the images from both FLIM and IVUS (yellow group). Outcome is co-registered FLIM and IVUS data (pink block).
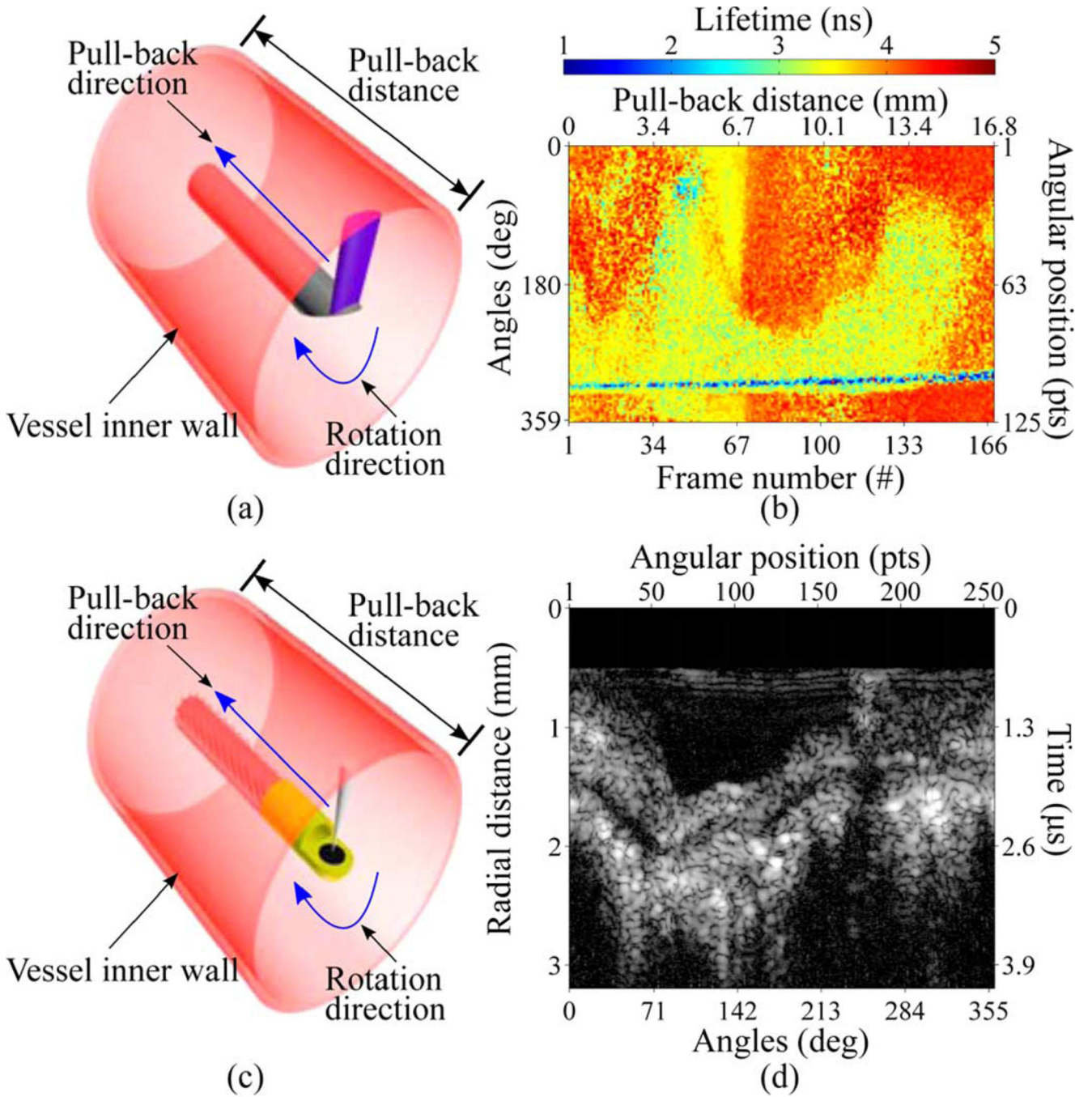
Fig. 2.
Pull-back principle for FLIM (a) and IVUS (c) systems. Each angular position of the side-viewing fiber corresponds to a single pixel in the 2-D map of lifetime values from the first channel (390/40 nm) of the FLIM system (b), while a full rotation of the IVUS transducer produces an IVUS frame (d).
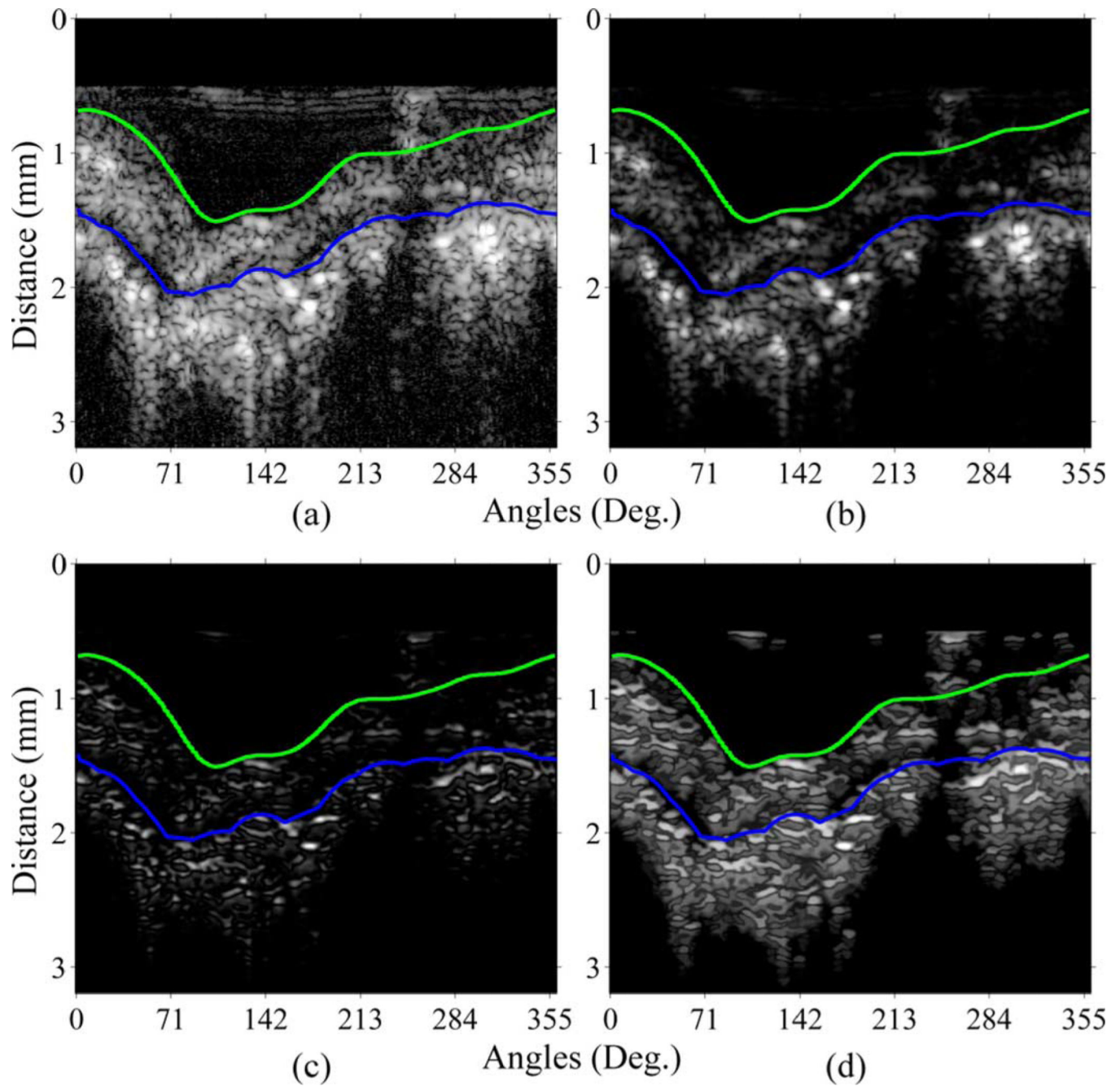
Fig. 3.
Input gray-scale polar IVUS image (a) was denoised with application of the Wiener filter (b) and the edge candidates were enhanced via estimation of the pixel separability metric, window size 21×3 pixels, (c). This image was further smoothed with two iterations of the alternating sequential filter and the result (intensity adjusted for visualization purposes) is shown in (d). True lumen/intima (green) and EEL (blue) boundaries are shown in all four images.
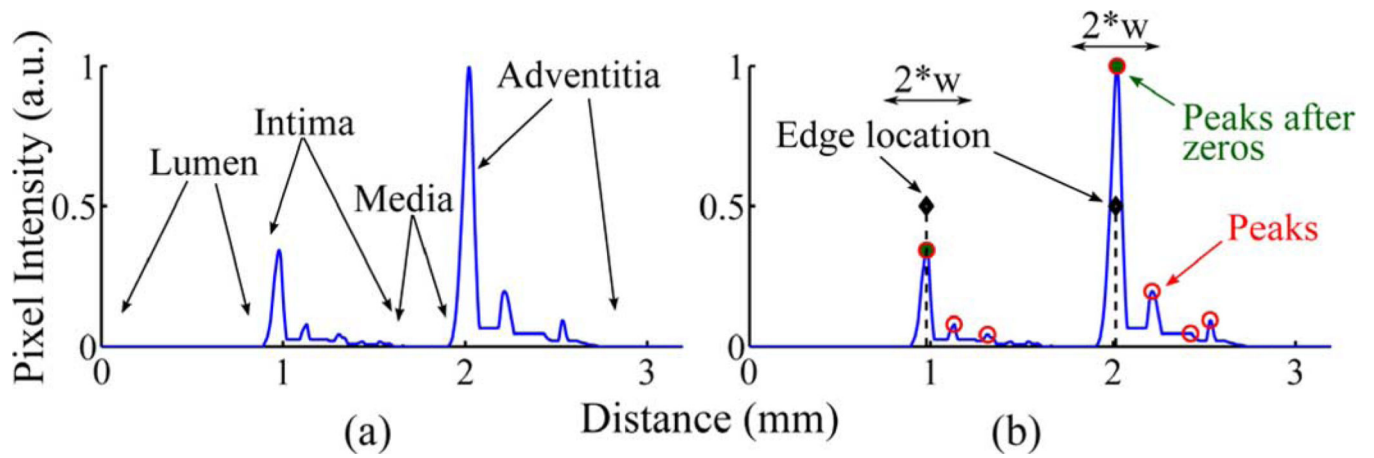
Fig. 4.
Lumen, intima, media, and adventitia as they appear on an A-line of a B-mode polar IVUS image (a). Each edge location corresponds to a peak that follows zero intensity pixels, while it is also delimited within ±w distances from the edge locations of the previous A-line and/or frame (b).
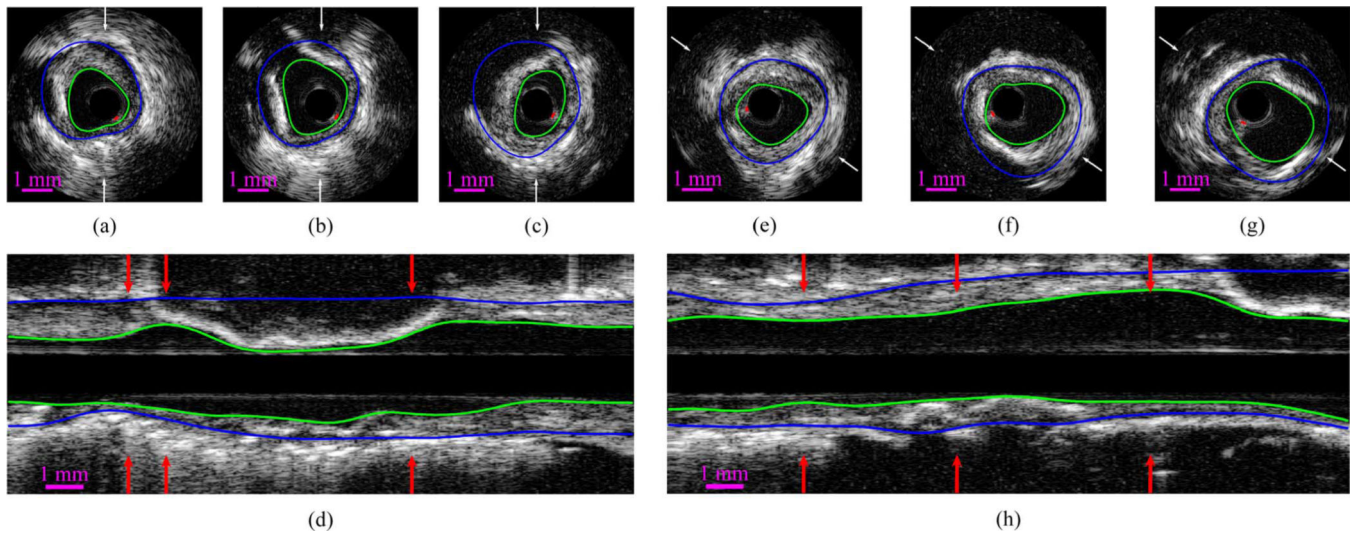
Fig. 5.
Frames with highlighted the lumen/intima (green) and EEL (blue) boundaries and the guide-wire artifact (red) from two pull-back sequences, (a)–(c) and (e)–(g). In these cross-sections with the white arrows are indicated the angles which have been selected for the corresponding longitudinal representations, (d) and (h). Red arrows in these views correspond to the cross-sections (a)–(c) and (e)–(g), ordered as they appear. In the attached video (clip1) are shown the segmentation results from two entire pull-back sequences.
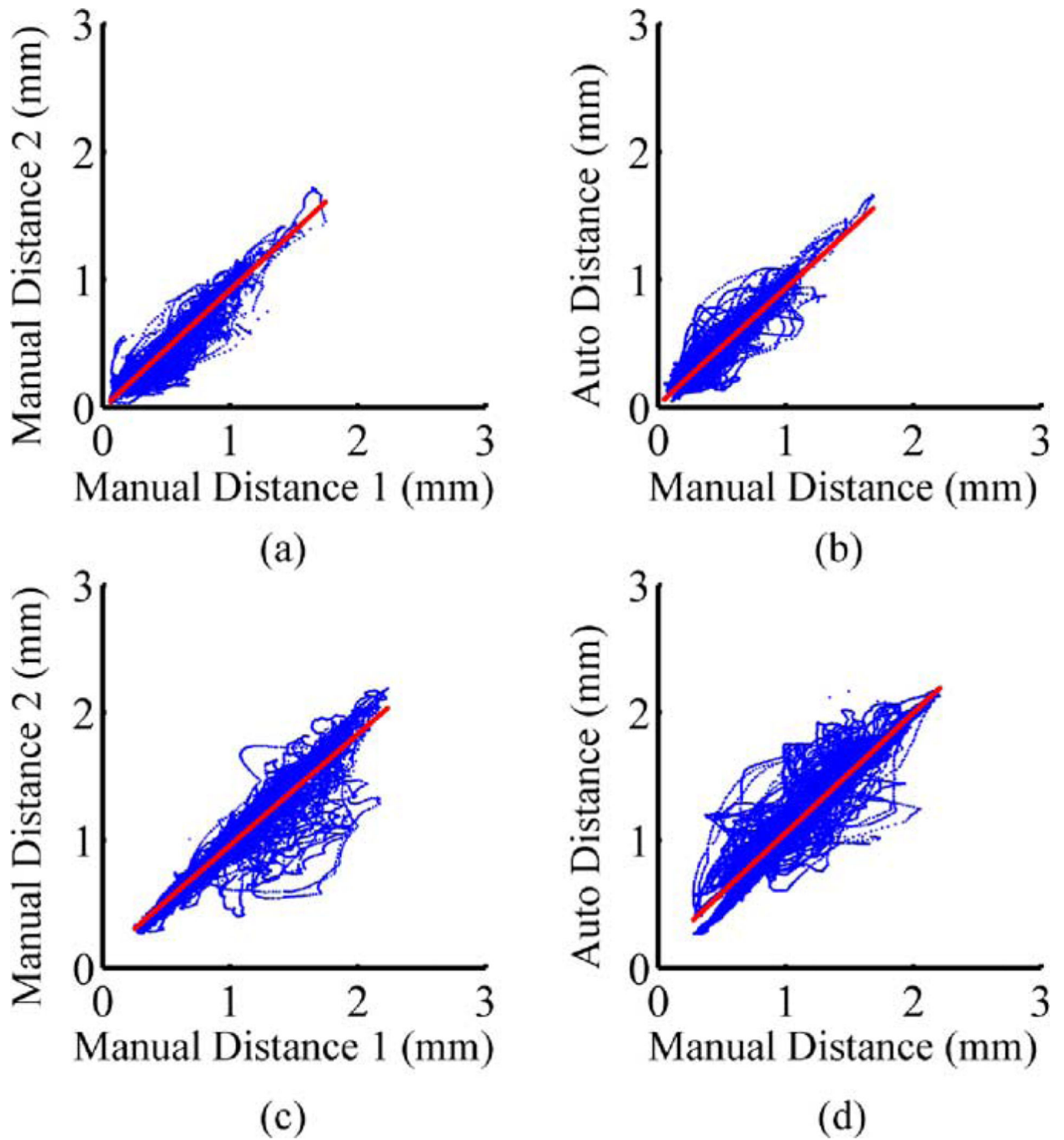
Fig. 6.
Linear regression results between the two manual segmentations, (a) and (c), and between the manual and the proposed automated segmentations, (b) and (d), for the lumen/intima, (a) and (b), and the EEL, (c) and (d), boundaries.
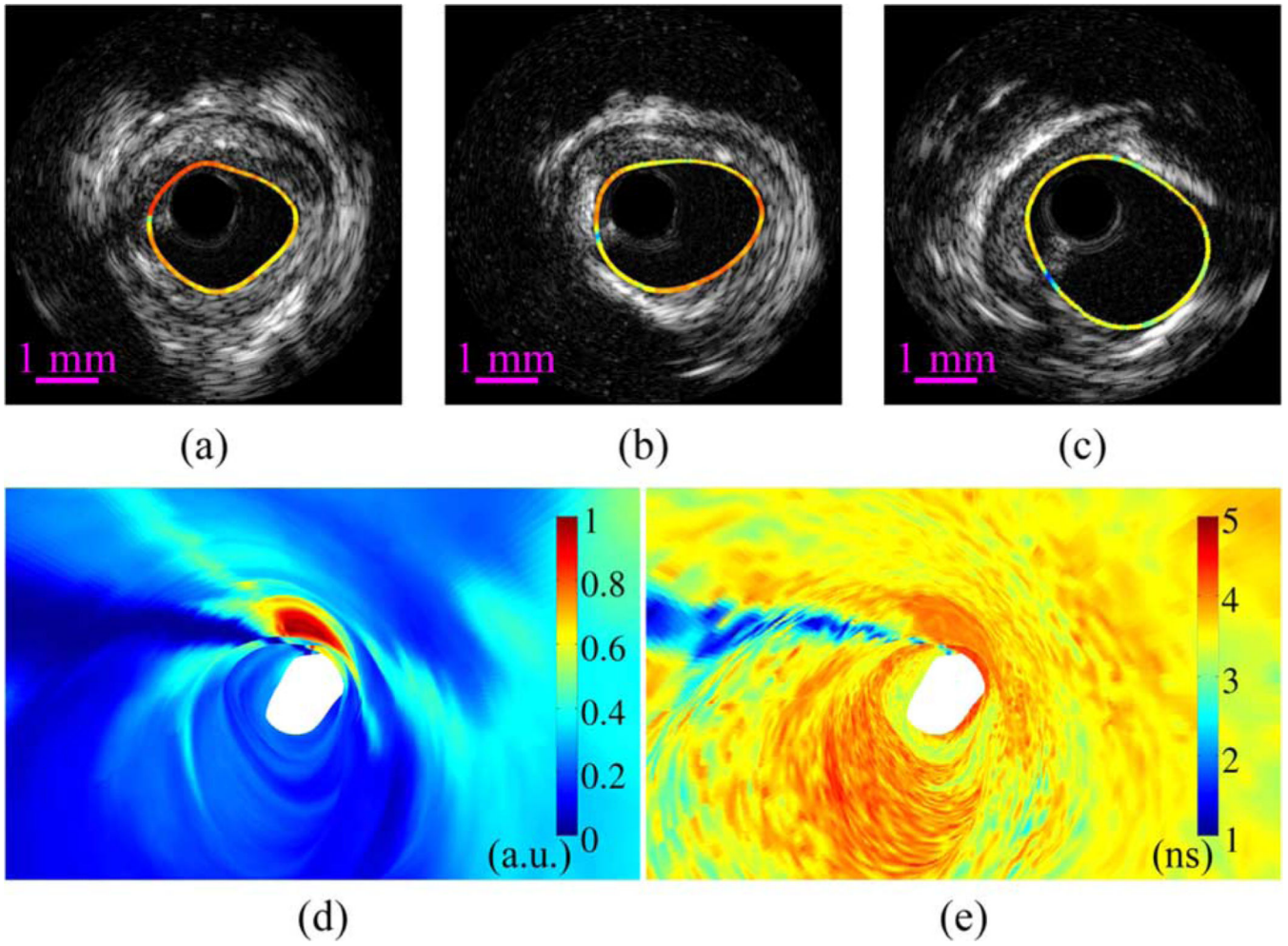
Fig. 7.
Three frames of Fig. 5(e)–(g) with lifetime values mapped onto the lumen/intima boundary (a)–(c). The normalized intensity (d) and the lifetime values (e) from the entire pull-back sequence, as reconstructed in fly-through visualization mode. The entire pull-back sequence with the mapped lifetime values in cross-sectional, longitudinal and three-dimensional reconstructions can be visualized in the second video (clip2), while the fly-through representation of both fluorescence intensity and lifetime values can be seen in the third attached video (clip3).
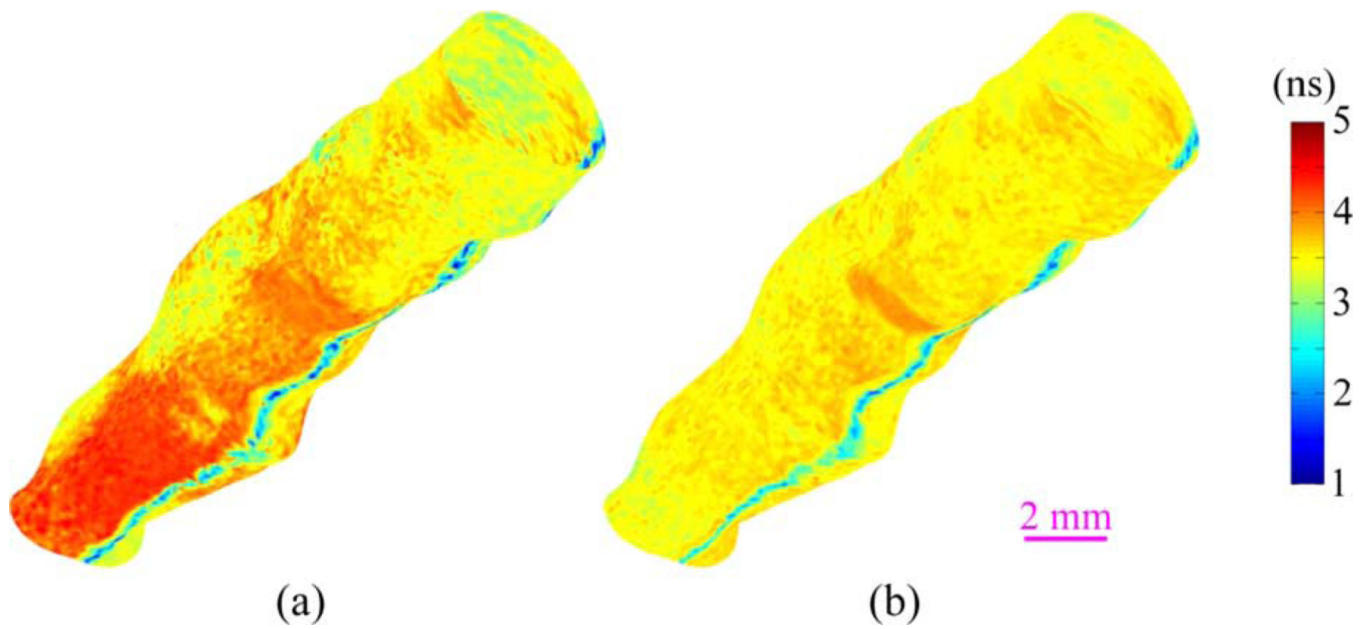
Fig. 8.
Lifetime values from the first (a) and the second (b) channels of the multimodal system mapped onto the lumen/intima surface from an entire pull-back sequence. Lifetime variations along the pull-back from the same of between different channels correspond to composition differentiations.
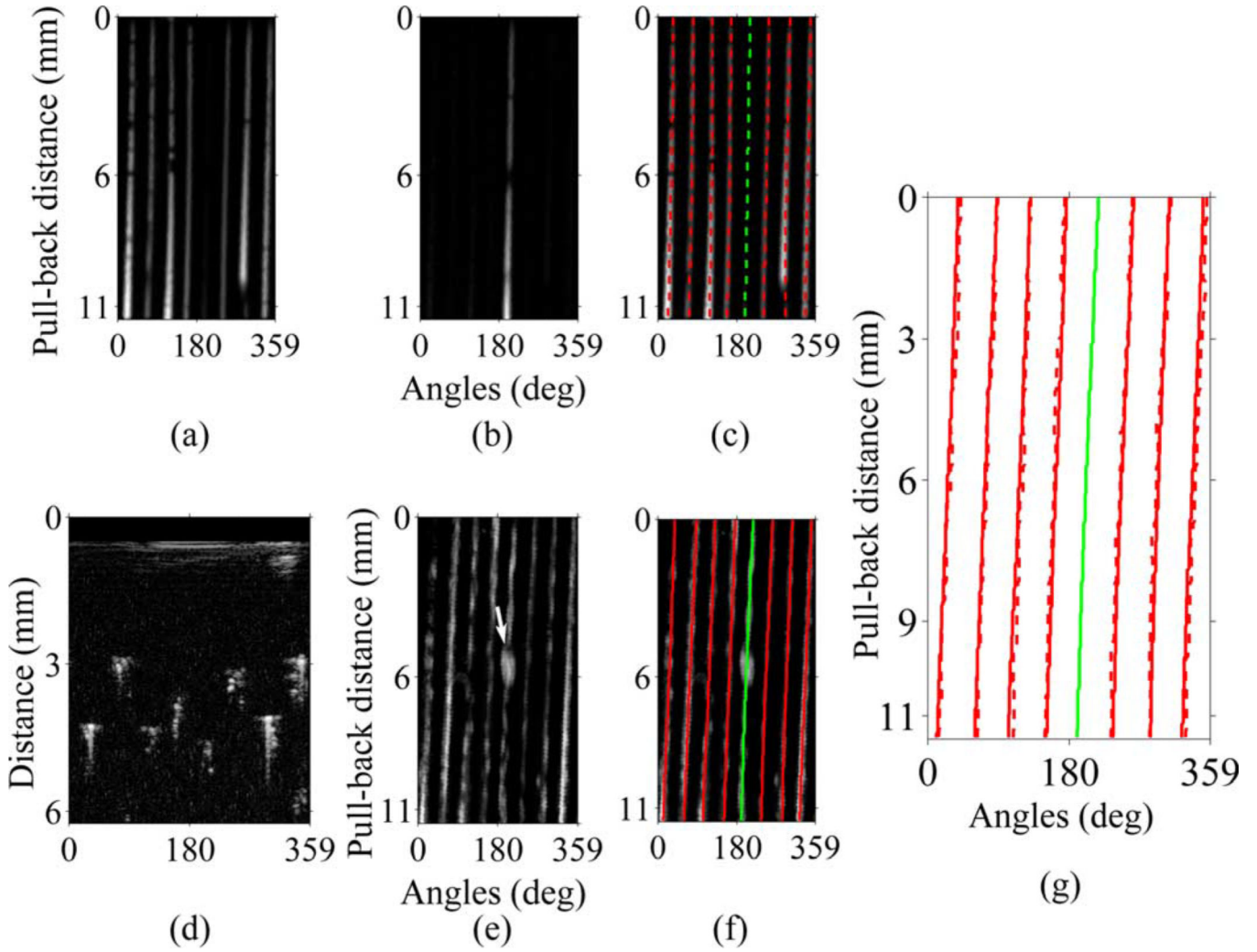
Fig. 9.
The 2-D map of the fluorescence intensity, in gray-scale, from the seven capillaries (a) and from the reference capillary (b) and the corresponding center lines (c). Acquired IVUS frames (d) where averaged per A-line and per frame, resulting in a 2-D map of IVUS intensities along the pull-back path (e). Metallic wire has been used to label the reference capillary, arrow in (e). Corresponding IVUS center lines (f) are used to align with the FLIM data and the outcomes of this procedure are shown in (g) with dashed lines for FLIM and solid for IVUS.

TABLE I

Lumen/Intima Segmentation Assessment. All Indexes are in mm and Mean Standard Deviations are Given

	Manual 1 vs Manual 2	Manual vs iMap	Manual vs Auto	iMap vs Auto
d_s	−0.05±0.09	0.03±0.09	0.03±0.08	−0.01±0.11
d_u	0.07±0.07	0.07±0.07	0.07±0.07	0.08±0.07
d_{rms}	0.12±0.05	0.12±0.05	0.11±0.05	0.13±0.06

TABLE II

EEL Segmentation Assessment. All Indexes are in mm and Mean Standard Deviations are Given

	Manual 1 vs Manual 2	Manual vs iMap	Manual vs Auto	iMap vs Auto
d_s	−0.06±0.15	0.03±0.13	−0.05±0.17	−0.08±0.22
d_u	0.09±0.13	0.08±0.10	0.11±0.14	0.15±0.19
d_{rms}	0.15±0.16	0.14±0.11	0.20±0.15	0.26±0.19